



Article

Research on Improving Energy Storage Density and Efficiency of Dielectric Ceramic Ferroelectric Materials Based on BaTiO₃ Doping with Multiple Elements

Jiaxuan Sun¹ and Yuanzhe Li^{2,3,*}

¹ Department of Physics, Shandong University, Jinan 250000, China; 201900100061@mail.sdu.edu.cn

² Carbon Neutrality Research Lab, China Academy of Art, Hangzhou 310002, China

³ School of Materials Science & Engineering, Nanyang Technological University, Singapore 639798, Singapore

* Correspondence: yuanzhe001@e.ntu.edu.sg

Abstract: In order to promote the research of green energy in the situation of increasingly serious environmental pollution, dielectric ceramic energy storage materials, which have the advantages of an extremely fast charge and discharge cycle, high durability, and have a broad use in new energy vehicles and pulse power, are being studied. However, the energy storage density of ordinary dielectric ceramic ferroelectric materials is low, so, in this paper, we have divided eight components based on BaTiO₃ (BT). Through the traditional solid phase sintering method, AB positions were replaced with various elements of different proportions to improve their energy storage density and the energy storage efficiency of BT-based ferroelectric materials. In this paper, we studied the results of XRD, Raman, ferroelectric, dielectric, and impedance tests of doped samples, and the best components were determined. The (1-x)BT-xBi(Mg_{1/3}Zn_{1/3}Ta_{1/6}Nb_{1/6})O₃ series of ceramics are made by the incorporation of five elements, Bi³⁺, Mg²⁺, Zn²⁺, Ta⁵⁺, and Nb⁵⁺. With the rising electric hysteresis loop of the doping amount x thin, the saturation polarization strength and residual polarization strength decrease, and the energy storage density rises first and then decreases. The dielectric characteristic after $x = 0.08$ showed a flat dielectric peak, indicating that the ferroelectric relaxation had been formed. The energy storage density and efficiency of the best component $x = 0.12$ reached 1.75 J/cm³ and 75%, respectively, and the Curie temperature was about -20 °C, so it has the potential to be used at room temperature.

Keywords: energy storage density; BaTiO₃; perovskite structure; phase transition; relaxation ferroelectric body



Citation: Sun, J.; Li, Y. Research on Improving Energy Storage Density and Efficiency of Dielectric Ceramic Ferroelectric Materials Based on BaTiO₃ Doping with Multiple Elements. *J. Compos. Sci.* **2023**, *7*, 233. <https://doi.org/10.3390/jcs7060233>

Academic Editor: Vincenza Brancato

Received: 11 May 2023

Revised: 24 May 2023

Accepted: 2 June 2023

Published: 5 June 2023



Copyright: © 2023 by the authors. Licensee MDPI, Basel, Switzerland. This article is an open access article distributed under the terms and conditions of the Creative Commons Attribution (CC BY) license (<https://creativecommons.org/licenses/by/4.0/>).

1. Introduction

With the developments of our current time, the negative impacts of traditional energy sources including fossil fuels such as coal, oil, and natural gas on the Earth's environment have been increasingly evident. This has spurred the exploration of alternative and environmentally friendly energy sources. After decades of efforts, various new energy sources such as photovoltaic, wind power, and geothermal energy have been developed and are being put into practical use. However, these types of energy sources that depend on power generation equipment are unable to provide sustainable and stable electricity generation. Therefore, one of the current hot research topics is how to effectively store and utilize these renewable energy sources using advanced storage devices and technologies [1,2].

1.1. Comparison of Energy Storage Material Performance

Power density refers to the rate at which energy can be supplied or extracted from an energy storage device. It is a measure of how quickly the device can deliver or receive energy. On the other hand, energy density refers to the amount of energy that can be stored in a given volume or mass of the storage device (Figure 1) [3]. It is a measure of how

much energy can be stored in the device. Dielectric energy storage capacitors, including those based on BT-based ferroelectric materials, are known for their fast charging and high discharge cycling rates, indicating a high power density. This means that they can quickly charge and discharge energy, making them suitable for applications where rapid energy delivery or extraction is required [2,3].

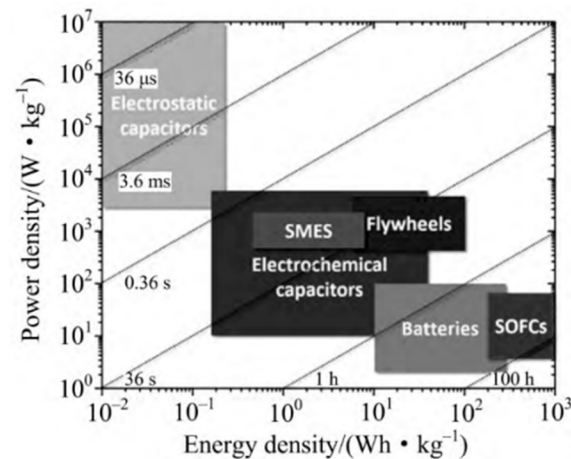


Figure 1. Relationship between power density and energy density in different energy storage devices. Reprinted with the permission from Yang, L.T.; Kong, X.; Li, F.; Hao, H.; Cheng, Z.; Liu, H.; Li, J.-F.; Zhang, S. Perovskite lead-free dielectrics for energy storage applications. *Prog. Mater. Sci.* 2019, 102, 72–108.

However, ordinary dielectric ceramic ferroelectric materials, including BaTiO₃ (BT), typically have a relatively low energy storage density. This means that they can store a limited amount of energy compared to other energy storage technologies such as batteries or supercapacitors. This limitation is a significant challenge in the practical application of dielectric energy storage capacitors, especially in energy-intensive applications such as new energy vehicles and pulse power systems [4]. To overcome this limitation, researchers have focused on improving the energy storage density and efficiency of BT-based ferroelectric materials through doping with various elements. Doping involves introducing impurities or additives into the material to modify its properties. By carefully selecting and incorporating suitable dopants, researchers aim to enhance the polarization response and dielectric properties of BT-based materials, thereby increasing their energy storage capacity.

Doping can lead to improved power density as well, as it can affect the charge–discharge rates and the overall electrical performance of the dielectric material. By optimizing the dopant concentration and composition, researchers can achieve a balance between power density and energy density in dielectric energy storage capacitors. This allows for faster charging and discharging rates while also increasing the overall amount of energy that can be stored. The research and development of dielectric ceramic energy storage materials, particularly those based on BT and doped variants, hold promise for addressing the energy storage challenges in various applications [2]. By improving the energy storage density and power density of dielectric capacitors, these materials can contribute to the development of more efficient and sustainable energy storage systems, supporting the transition towards green energy solutions [4].

1.2. Classification of Energy Storage Dielectric Materials

Dielectric materials used for energy storage can be classified into four types: linear dielectrics, ferroelectrics, relaxor ferroelectrics, and antiferroelectrics. Linear dielectrics (Figure 2):

- (a) Linear dielectrics are materials that exhibit a linear relationship between the applied electric field and the resulting polarization. These materials have a low dielectric constant and do not possess any inherent polarization or ferroelectric properties. They

are commonly used in capacitors for their insulation and energy storage capabilities [5]. However, their energy storage density is relatively low compared to other dielectric materials due to their limited polarization response.

- (b) **Ferroelectrics:** Ferroelectric materials are dielectrics that exhibit spontaneous electric polarization that can be reversed by an external electric field. They have a high dielectric constant and hysteresis behavior, making them suitable for energy storage applications. The polarization in ferroelectrics is typically induced by a phase transition and is maintained even after the removal of the electric field. This property allows for high energy storage density and makes ferroelectrics desirable for capacitors in various electronic devices.
- (c) **Relaxor ferroelectrics:** Relaxor ferroelectrics are a special class of ferroelectric material that exhibit a broad and frequency-dependent dielectric response. Unlike traditional ferroelectrics, their polarization response is more disordered and relaxes over a wide temperature range. Relaxor ferroelectrics have high energy storage densities and can withstand high electric fields, making them useful in applications where high energy storage and high-power density are required, such as pulsed power systems.
- (d) **Antiferroelectrics:** Antiferroelectric materials are dielectrics that exhibit alternating regions of electric polarization with opposite directions. Unlike ferroelectrics, antiferroelectrics have zero net polarization even in the presence of an external electric field. However, they can store energy by switching the polarization direction, similar to ferroelectrics. Antiferroelectrics have shown potential for high energy storage density and fast charge–discharge rates, making them promising candidates for capacitors in applications that require rapid energy transfer.

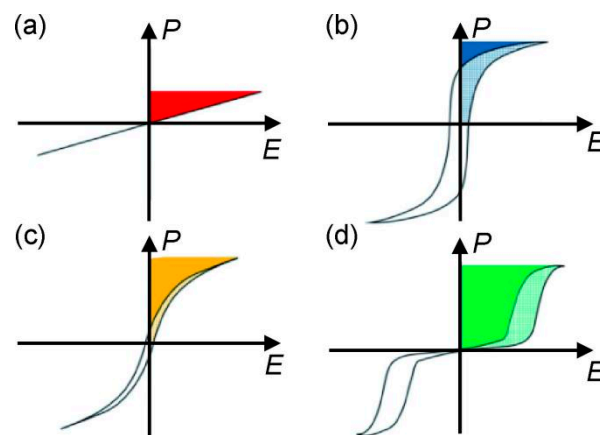


Figure 2. Four types of dielectric energy storage materials: (a) linear dielectrics, (b) ferroelectrics, (c) relaxor ferroelectrics, and (d) antiferroelectrics. Reprinted with the permission from Liu, Z.; Lu, T.; Ye, J.M.; Wang, G.; Dong, X.; Withers, R.; Liu, Y. Antiferroelectrics for energy storage applications: A review. *Adv. Mater. Technol.* 2018, 3, 1800111.

Each of these types of dielectric energy storage material offers unique properties and advantages for different applications. The choice of material depends on specific requirements such as energy storage density, power density, dielectric constant, hysteresis behavior, and operating conditions. Researchers continue to explore and optimize these materials to enhance their energy storage capabilities and develop more efficient dielectric energy storage devices for various technological advancements. Among these, ferroelectric materials have gained significant attention due to their unique properties such as fast charge and discharge cycles, high durability, and broad applicability in new energy vehicles and pulse power systems [5]. However, conventional ferroelectric materials, such as pure BaTiO₃ (BT), have limitations in terms of energy storage density. To overcome this challenge, researchers have focused on doping BT with various elements to improve its energy storage properties [6,7]. In this paper, we present a comprehensive study on the enhancement of

energy storage density and efficiency by incorporating five elements, namely, Bi^{3+} , Mg^{2+} , Zn^{2+} , Ta^{5+} , and Nb^{5+} , into the $(1-x)\text{BT}-x\text{Bi}(\text{Mg}_{1/3}\text{Zn}_{1/3}\text{Ta}_{1/6}\text{Nb}_{1/6})\text{O}_3$ series of ceramics.

In this study, the focus is on investigating and enhancing the potential application of relaxor ferroelectric ceramics. The researchers selected BaTiO_3 , a classic ferroelectric material, as the base and doped it with Bi^{3+} , Mg^{2+} , Zn^{2+} , Ta^{5+} , and Nb^{5+} to form a binary solid solution with BT. By adjusting the doping proportions, the researchers aimed to improve the breakdown strength, energy storage efficiency, and reduce the Curie temperature of the resulting relaxor ferroelectric materials [8]. These modifications are essential to make the materials suitable for ambient temperature conditions, thus expanding their potential applications. To achieve these goals, various experimental techniques were employed. The researchers analyzed the microstructural features of the doped samples and studied their dielectric properties, electrical impedance, and ferroelectric behavior. By gathering and analyzing the experimental data, the team aims to determine the optimal composition that can yield the desired properties [9].

The ultimate objective of this study is to unlock the application potential of relaxor ferroelectric ceramics by identifying the composition that exhibits improved performance in terms of breakdown strength, energy storage efficiency, and suitability for ambient temperature conditions. This research has the potential to contribute to the development and advancement of relaxor ferroelectric materials for various technological applications, including energy storage devices, capacitors, and other electronic systems.

2. Literature Review

2.1. Basic Principles of Dielectric Energy Storage

2.1.1. Dielectrics and Polarization

Dielectric materials, in the context of electrical engineering and physics, refer to insulating materials that have the ability to store energy in the form of a polarized charge when subjected to an external electric field. The polarization intensity, denoted as P , is a fundamental parameter used to describe the response of dielectric materials to an applied electric field (Equation (1)). The polarization intensity, P , represents the total dipole moment per unit volume within the dielectric material. It is the sum of the dipole moments of individual atoms or molecules that make up the material. When an external electric field is applied, the dipole moments within the dielectric material align themselves with the field, resulting in a net polarization and the storage of electrical energy [9,10].

$$P = \frac{\sum_i p_i}{\Delta V} \quad (1)$$

and is related to the dielectric constant as follows (Equations (2) and (3)):

$$P = (\epsilon_r - 1)\epsilon_0 E \quad (2)$$

$$\chi = (\epsilon_r - 1) \quad (3)$$

ϵ_r is the relative permittivity (dielectric constant), ϵ_0 is the vacuum permittivity, and χ is the polarization ratio. The electric susceptibility, χ , is specific to each dielectric material and characterizes its ability to polarize under the influence of an electric field [11]. It depends on factors such as the molecular or atomic structure of the material, its composition, and temperature.

Dielectric materials find numerous applications in electronic devices, capacitors, insulation systems, and energy storage devices. They are used to enhance electrical insulation, reduce signal loss in transmission lines, and increase the capacitance of capacitors, among other functions [12]. The choice of dielectric material depends on its specific electrical properties, such as permittivity, breakdown strength, and temperature stability, to suit the requirements of the intended application.

2.1.2. Parallel Plate Capacitor

This configuration allows for the storage of an electric charge and the generation of an electric field between the plates (Equation (4)). Equation (4) represents the relationship between the stored charge (q), applied voltage (U), plate area (S), and the distance between the plates (d). The constant C_0 represents the capacitance of the parallel plate capacitor when the material between the plates is a vacuum or air, and ϵ_0 is the vacuum permittivity. It can be expressed as

$$C_0 = \frac{q}{U} = \frac{\epsilon_0 S}{d} \quad (4)$$

When a voltage is applied across the parallel plate capacitor, one plate becomes positively charged while the other plate becomes negatively charged. This separation of charges creates an electric field between the plates [13]. The magnitude of the electric field is directly proportional to the voltage applied and inversely proportional to the distance between the plates. Equation (5) represents the relationship between the stored charge (q), applied voltage (U), plate area (S), distance between the plates (d), and the relative permittivity (ϵ_r) of the material between the plates. The term σ_e represents the electric charge density, and E represents the electric field magnitude between the plates. The equation can be rewritten as follows, where C represents the capacitance of the parallel plate capacitor:

$$C = \frac{q}{U} = \frac{\sigma_e}{Ed} = \frac{(1 + \chi)\epsilon_0 S}{d} = \epsilon_r C_0 \quad (5)$$

The capacitance (C) of the parallel plate capacitor is a measure of its ability to store charge and is determined by several factors. It is directly proportional to the area of the plates (S) and the permittivity (ϵ) of the material between the plates. Additionally, the capacitance is inversely proportional to the distance (d) between the plates [14,15].

2.1.3. Dielectric Loss

Under the influence of an external electric field, the charges within a dielectric material experience a displacement or movement. During this polarization process, energy losses occur due to various mechanisms within the material. These losses result in the dielectric material exhibiting a slight lag in polarization response compared to changes in the external electric field. One of the significant mechanisms causing energy losses in a dielectric material is the collision between electrons and atomic nuclei [16]. These collisions generate heat and dissipate energy, leading to a reduction in the efficiency of the polarization process. As a result, the dielectric material experiences a dissipation of energy, which is characterized by dielectric loss [17].

Dielectric loss is quantified by a parameter known as the dielectric loss tangent, often denoted as $\tan \delta$. This parameter represents the ratio of the energy dissipated as heat to the energy stored in the dielectric material per cycle of the applied electric field. Mathematically, $\tan \delta$ is given by (Equation (6)):

$$\tan \delta = (\text{Power dissipated as heat}) / (\text{Power stored in the dielectric}) \quad (6)$$

The dielectric loss tangent, $\tan \delta$, is also referred to as the dielectric loss angle. It represents the phase angle, δ , between the displacement of polarization and the external electric field. The value of $\tan \delta$ is typically small for good dielectric materials, indicating low energy losses and efficient energy storage [18–29]. Understanding dielectric loss and its associated angle is crucial for assessing the performance and efficiency of dielectric materials in various applications. By minimizing dielectric loss and optimizing dielectric properties, engineers can design more efficient electrical systems and devices.

2.1.4. Hysteresis Loop and Spontaneous Polarization

Ferroelectricity is a result of the presence of spontaneous polarization within the material. In certain crystals, the centers of positive and negative charges in the unit cell do not coincide, resulting in the formation of a dipole moment. This polarization state that

exists in the absence of an external electric field is called spontaneous polarization [20]. Spontaneous polarization inside the crystal is divided into small regions called domains, where the polarization directions are not aligned. As shown in Figure 3 [21], in the absence of an applied external electric field (E), the domains in a ferroelectric material are typically multi-domain, randomly distributed. When an electric field (E) is applied, the original domains disappear, and a single-domain structure is formed, resulting in spontaneous polarization [21,22]. The phenomenon of spontaneous polarization requires the application of a reverse electric field to bring the polarization intensity P back to zero.

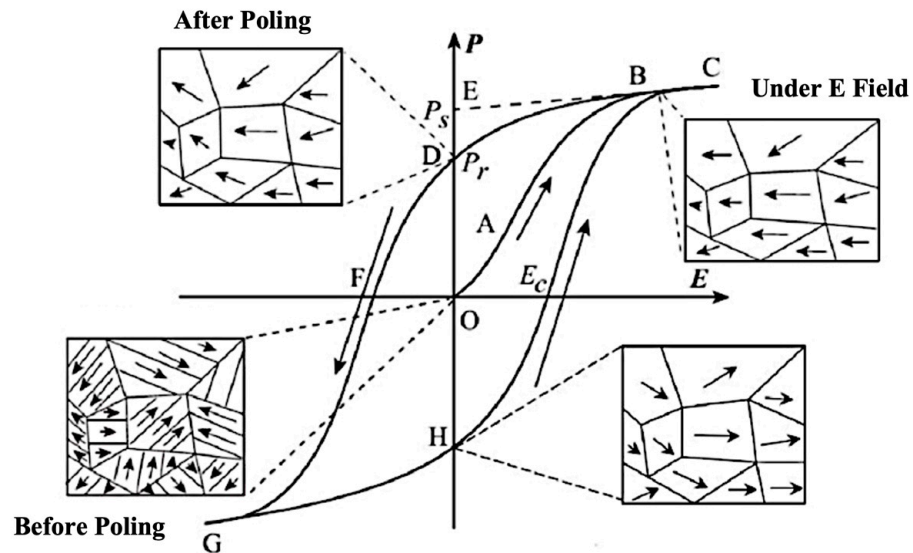


Figure 3. Hysteresis loop and domains in ferroelectric material. Reprinted with the permission from Jin, L.; Li, F.; Zhang, S. Decoding the Fingerprint of Ferroelectric Loops: Comprehension of the Material Properties and Structures. *J. Am. Ceram. Soc.* 2014, 97, 1.

2.1.5. Calculation of Energy Storage Density

The electric displacement vector can be expressed as a sum of the product of the permittivity of free space ϵ_0 , the relative permittivity ϵ_r , the electric field strength E , and the polarization intensity P (Equations (7) and (8)):

$$D = \epsilon_0 \epsilon_r E = \epsilon_0 E + P \tag{7}$$

whereas

$$P = (\epsilon_r - 1) \epsilon_0 E \tag{8}$$

Due to the high relative permittivity (ϵ_r) of the BaTiO_3 material used in this study, $D \approx P$.

In the context of dielectric energy storage materials, the energy storage density can be calculated using the following formula:

$$W = \int E dD \approx \int E dP \tag{9}$$

Using Equation (9), the energy storage density can be approximated as the integral of the product of the electric field strength E and the polarization intensity P . This equation represents the amount of energy that can be stored per unit volume of the dielectric material under the influence of an external electric field (Figure 4) [15,23].

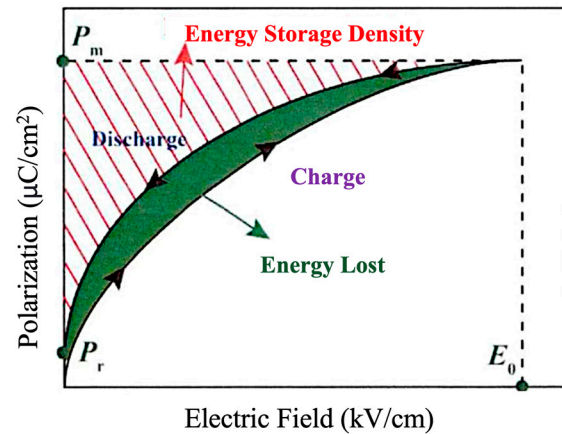


Figure 4. Schematic of energy density during charging and discharging of a capacitor. Reprinted with the permission from Wang, X. Study on the Dielectric Energy Storage Characteristics of Barium Titanate-Based Ferroelectric Ceramics. Ph.D. Thesis, Shandong University, Jinan, China, 2020.

By studying the dielectric properties and energy storage behavior of various materials, engineers can develop more efficient and high-performance dielectric materials for energy storage applications. The following equations (Equations (10)–(12)) describe key aspects of the energy storage process [20,24]:

(a) Charging process

Equation (10) represents the work executed (W) during the charging process of a dielectric material. The integral calculates the area under the electric field (E) versus polarization (P) curve, where P_m is the maximum polarization achieved during charging. This equation quantifies the amount of energy required to charge the dielectric material.

$$W = \int_0^{P_m} E dP \tag{10}$$

(b) Discharging process

Equation (11) describes the work executed during the discharging process of the dielectric material. The integral calculates the area under the electric field versus the polarization curve for the range between the remanent polarization (P_r) and the maximum polarization (P_m). This equation quantifies the energy released during the discharge phase.

$$W_{rec} = \int_{P_r}^{P_m} E dP \tag{11}$$

(c) Energy efficiency

Equation (12) provides a measure of the energy efficiency (η) of the dielectric energy storage system. It is calculated by dividing the work executed during the discharging process (W_{rec}) by the work executed during the charging process (W) and multiplying by 100%. This equation expresses the percentage of energy that is successfully recovered during the discharge process relative to the energy initially stored in the dielectric material.

$$\eta = \frac{W_{rec}}{W} \times 100\% \tag{12}$$

2.2. Structural Characteristics of BaTiO₃-Based Relaxor Ferroelectric Ceramics

BaTiO₃ is a well-known ferroelectric material with a perovskite structure represented by the chemical formula ABO₃. It has been extensively studied since the 1940s [3]. BT is considered a room-temperature ferroelectric material and possesses several advantages, including a high dielectric constant, low equivalent series resistance, good thermal stability, and high reliability. These properties make it suitable for use as a dielectric in medium- to low-frequency capacitors where large capacitance is required and temperature variation is not significant [16].

However, conventional BT-based ferroelectric materials have certain limitations. They tend to have a relatively large remanent polarization (P_r) and exhibit relatively low dielectric breakdown strength [4]. These characteristics make them unsuitable for large-scale energy storage applications. To unlock the energy storage potential of BT, chemical doping techniques can be employed. This involves substituting Ba^{2+} or Ti^{4+} ions with equivalent or valence-different ions, resulting in the formation of relaxor ferroelectric materials. This doping process can significantly enhance the energy storage density and efficiency of BT materials [24].

The crystal structure of BaTiO_3 undergoes various structural distortions at different temperatures, including the hexagonal, cubic, tetragonal, orthorhombic, and trigonal phases [16]. In the perovskite structure, Ba^{2+} ions occupy the corner positions of the cube (A-site), while the O^{2-} ions occupy the face-centered positions forming oxygen octahedra. The body center (B-site) is occupied by Ti^{4+} ions. Below 120°C , the crystal undergoes a transition to the tetragonal phase. As the temperature decreases, the thermal kinetic energy of the Ti^{4+} ions at the body's center decreases. At a specific temperature, when the irregular motion of the Ti^{4+} ions aligns with a particular O^{2-} ion, the remaining energy is insufficient to overcome the electric field forces between them. This leads to a displacement of the ions, and they reach a new equilibrium position. As a result, the O^{2-} ions also undergo displacement, causing a slight elongation along the c-axis and a slight contraction along the a- and b-axes. This polarization leads to the spontaneous polarization of the crystal along the c-axis, resulting in the phenomenon known as spontaneous polarization [25].

By understanding the crystal structure and the behavior of BT, researchers can explore doping techniques to modify its properties and enhance its energy storage capabilities. Chemical doping opens up possibilities for tailoring the performance of BT-based materials and expanding their potential applications in energy storage systems.

In Equation (13), t represents the tolerance factor, which is a parameter used to describe the distortion and relaxation behavior in perovskite structures. The tolerance factor is calculated using the radii of the A-site ions (R_A), B-site ions (R_B), and oxygen ions (R_O).

$$t = \frac{R_A + R_O}{\sqrt{2}(R_B + R_O)} \quad (13)$$

The tolerance factor value is used to assess the structural stability and distortion in perovskite materials [16]. Typically, a reasonable range for the tolerance factor is $0.77 < t < 1.1$. To induce relaxation behavior and modify the tolerance factor, the substitution of ions can be performed. In this case, the Ba^{2+} ion with a radius of 1.61 \AA is substituted with a smaller ion at the A-site.

One commonly used ion for substitution is Bi^{3+} with a radius of 1.31 \AA . The substitution of Bi^{3+} for Ba^{2+} reduces the value of t , leading to relaxation in the material structure.

However, when substituting Ba^{2+} with Bi^{3+} , the appropriate pairing of elements is required at the B-site to maintain charge balance. In this study, the B-site doping involved a mixture of Mg^{2+} , Zn^{2+} , Ta^{5+} , and Nb^{5+} in a ratio of 2:2:1:1. This combination resulted in the formation of a BT–Bi binary solid solution, where BT represents the base material BaTiO_3 . By carefully selecting the ions for substitution and adjusting their ratios, researchers can modify the tolerance factor and induce relaxation behavior in the material, thereby influencing its dielectric and energy storage properties [7,15].

3. Research Methodology

3.1. Sample Preparation

The raw materials, including BaCO_3 , TiO_2 , Bi_2O_3 , MgO , ZnO , Ta_2O_5 , and Nb_2O_5 (all purity $\geq 99.5\%$) were sourced from Sigma-Aldrich (St. Louis, MI, USA). Ensuring the high purity of these raw materials was essential for the accurate investigation of the peak shift effect in BaTiO_3 (BT) ferroelectric ceramics through doping with transition elements.

In the sample preparation process, the weighed raw materials were mixed using a high-energy ball milling technique with a milling speed of 1000 rpm, a ball size of 6 mm,

and a milling time of 3 h. This high-energy ball milling technique, performed using Planetary Ball Mill PULVERISETTE 7 Premium Line, allowed for effective mixing and ensured homogeneity of the resulting ceramic samples.

3.2. Sintering Process

After the powder mixture was prepared, it was subjected to a sintering process. The powder mixture was placed in a suitable crucible and heated in a controlled atmosphere furnace. The sintering temperature and duration were optimized based on previous studies and experimental parameters [18]. The heating rate and cooling rate were carefully controlled to minimize the occurrence of defects and ensure the formation of a dense ceramic structure.

3.3. Characterization Techniques

Various characterization techniques were employed to analyze the properties of the doped BT-based ceramic samples. These techniques included.

3.3.1. X-ray Diffraction (XRD)

XRD analysis was performed using a Bruker D8 Series to determine the crystal structure and phase composition of the ceramic samples of $(1-x)\text{BT}-x\text{Bi}(\text{Mg}_{1/3}\text{Zn}_{1/3}\text{Ta}_{1/6}\text{Nb}_{1/6})$. The XRD patterns were obtained using a high-resolution X-ray diffractometer. The collected data were analyzed using appropriate software to identify the presence of desired phases and to calculate lattice parameters [18].

3.3.2. Raman Spectroscopy

Raman spectroscopy was performed using Thermo Scientific DXR 3, typically in the visible or near-infrared range, and the scattered light was collected and analyzed. The acquired Raman spectra were carefully processed and background corrected to enhance the signal-to-noise ratio. Finally, the Raman peaks were identified and assigned based on their vibrational modes, allowing for the determination of the lattice dynamics and structural properties of the materials. The obtained Raman data provide valuable insights into the composition-dependent phase transitions, phonon behavior, and lattice distortions, contributing to a comprehensive understanding of the material's functional properties [17,20].

3.3.3. Dielectric Measurements

Dielectric measurements were conducted to evaluate the dielectric properties of the doped BT-based ceramics. A precision impedance analyzer was used to measure the dielectric constant (ϵ) and dielectric loss ($\tan \delta$) as functions of temperature and frequency [24]. The measurements were performed over a range of temperatures and frequencies to capture the behavior of the ceramics.

3.3.4. Impedance Measurements

The impedance data were collected at various temperatures and frequencies to investigate the dielectric response of the material as a function of composition. The obtained impedance spectra were then analyzed using appropriate equivalent circuit models, such as the Cole–Cole model, to extract valuable information about the dielectric properties, including the dielectric constant, dielectric loss, and electrical conductivity. This methodology enabled a comprehensive understanding of the dielectric's behavior and provided insights into its potential applications in various electronic devices [25].

3.3.5. Polarization Measurements

Polarization measurements were carried out to analyze the ferroelectric properties of the ceramic samples. A ferroelectric tester was used to measure the polarization–electric field hysteresis loops and determine the remanent polarization (P_r) and coercive field (E_c).

These measurements provided insights into the ferroelectric behavior and polarization stability of the ceramics [26].

3.3.6. Energy Storage Performance

To analyze the storage performance of the compositions, a comprehensive testing method was employed. First, the ferroelectric properties were evaluated using a P - E measurement. The samples were subjected to a series of electric fields ranging from low to high, and the polarization response was recorded. The maximum polarization intensity (P_{max}) and remanent polarization intensity (P_r) were determined from the hysteresis loops obtained [12]. Additionally, the breakdown field strength was measured to assess the susceptibility of the compositions to breakdown. Furthermore, the energy storage characteristics were investigated through the calculation of energy density and efficiency. The energy density was determined by integrating the area under the P - E curve, while the efficiency was calculated by comparing the energy stored and released during the charging and discharging processes. The testing was performed for various compositions with different doping levels, allowing for a comparative analysis of their storage performance.

4. Results and Discussion

4.1. XRD and Raman Spectrum Analysis

Figure 5 presents the X-ray diffraction spectrum of $(1-x)\text{BT}-x\text{Bi}(\text{Mg}_{1/3}\text{Zn}_{1/3}\text{Ta}_{1/6}\text{Nb}_{1/6})$. Figure 5a shows the spectrum in the 20 – 80° testing angle range, and the diffraction pattern is in good agreement with the results of the standard card PDF#31-0174 [9]. The diffraction patterns exhibit a perovskite structure for different doping proportions, indicating the successful incorporation of $x\text{Bi}(\text{Mg}_{1/3}\text{Zn}_{1/3}\text{Ta}_{1/6}\text{Nb}_{1/6})$ elements into the BT lattice. Figure 5b zooms in on the range of 45 – 46.5° and reveals a change in the shape and position of the (200) diffraction peak around 45.5° as the doping level (x) increases. For $x \leq 0.04$, a split double peak is observed, indicating the presence of a tetragonal phase. For $x \geq 0.04$, the double peak transitions into a single diffraction peak (2 0 0), indicating a transformation from the tetragonal phase to a pseudocubic phase [15]. As the doping level increases, the (2 0 0) diffraction peak gradually shifts to lower angles, indicating an increase in the lattice constant as per the Bragg equation.

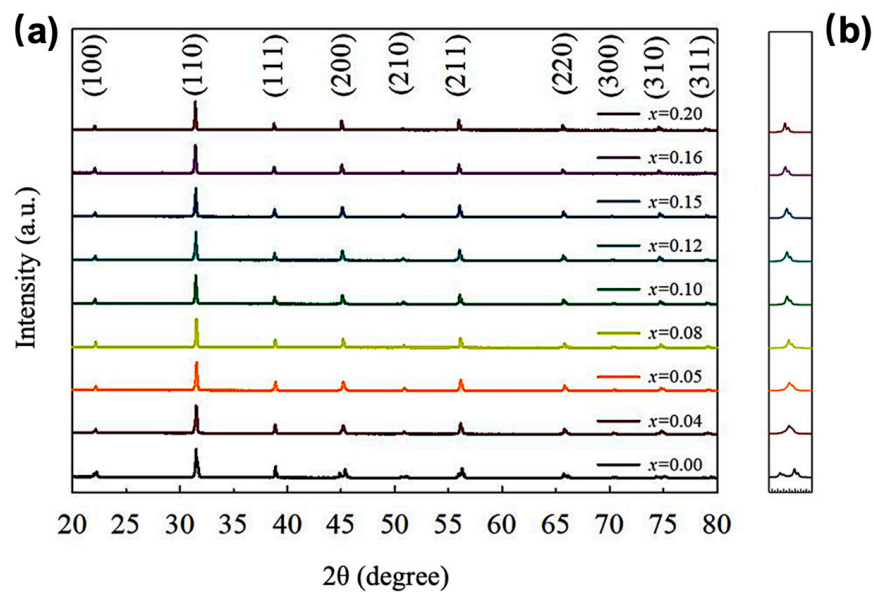


Figure 5. X-ray diffraction spectrum of $(1-x)\text{BT}-x\text{Bi}(\text{Mg}_{1/3}\text{Zn}_{1/3}\text{Ta}_{1/6}\text{Nb}_{1/6})$ capacitor: (a) 20 – 80° testing angle range and (b) zooming in on the range of 45 – 46.5° .

Figure 6 displays the Raman spectrum of $(1-x)\text{BT}-x\text{Bi}(\text{Mg}_{1/3}\text{Zn}_{1/3}\text{Ta}_{1/6}\text{Nb}_{1/6})$ in the wavenumber range of 100 – 1000 cm^{-1} . With the increase in doping proportion, particularly from $x = 0$ to $x = 0.04$, significant structural changes are observed. At $x = 0$, the main

characteristic peaks are located near 260, 304, 516, and 716 cm^{-1} , corresponding to the four typical phonon modes of pure BaTiO_3 [18,19]. After introducing the dopants, the characteristic peak of the tetragonal phase at 260 cm^{-1} disappears. The peaks at 304 cm^{-1} and 716 cm^{-1} broaden gradually, attributed to the disordered displacement of Ti^{4+} ions in the Ti-O octahedra, indicating a decrease in the long-range order of the ferroelectric BaTiO_3 structure [20]. As x increases, two new characteristic peaks related to A-O bond vibrations appear at 113 cm^{-1} and 180 cm^{-1} , indicating the formation of ion-enriched regions of Ba^{2+} or Bi^{3+} [22]. The flattening and broadening of the characteristic peaks at 516 cm^{-1} and 716 cm^{-1} confirm the presence of Ti^{4+} cluster enrichments in the short-range structure even after the long-range ordered structure of Ti^{4+} at the B-site is disrupted [23].

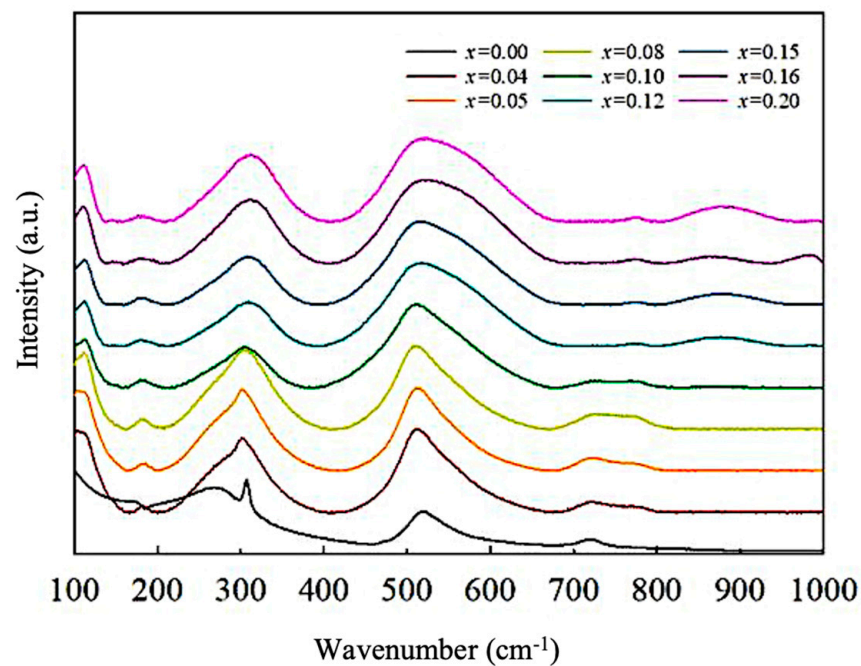


Figure 6. Raman spectrum of $(1-x)\text{BT}-x\text{Bi}(\text{Mg}_{1/3}\text{Zn}_{1/3}\text{Ta}_{1/6}\text{Nb}_{1/6})$ in the wavenumber range of 100–1000 cm^{-1} .

4.2. Dielectric Behavior Analysis

In order to investigate the changes in the dielectric behavior of BT ceramics after doping, this section presents a comparative graph of the dielectric constant and dielectric loss for the range of $0.04 \leq x \leq 0.20$, $1 \text{ kHz} \leq f \leq 1 \text{ MHz}$, and $-50 \text{ }^\circ\text{C} \leq t \leq 150 \text{ }^\circ\text{C}$.

From Figure 7, it can be observed that the image at $x = 0.04$ still exhibits a sharp dielectric peak, and the dielectric constant rapidly changes after approaching the Curie temperature at around $T_c = 20 \text{ }^\circ\text{C}$, showing no frequency dispersion. Overall, the dielectric constant demonstrates the typical behavior of a regular ferroelectric material such as BT, although the dielectric loss is significantly reduced. However, when $x \geq 0.08$, the dielectric peak in the image becomes noticeably flat and gentle, and the dielectric constant remains at a low level within the temperature range of the test. As x increases, the dielectric constant decreases: at $x = 0.08$, the dielectric constant at 1 kHz is approximately 2200, while at $x = 0.16$, it reduces to only 800. This indicates the presence of the characteristic diffuse phase transition of relaxor ferroelectric materials. Simultaneously, the Curie temperature shifts to higher temperatures as the frequency increases. For example, at $x = 0.08$, the Curie temperature at 1 kHz is approximately $-35 \text{ }^\circ\text{C}$, while at 1 MHz, it is around $18 \text{ }^\circ\text{C}$.

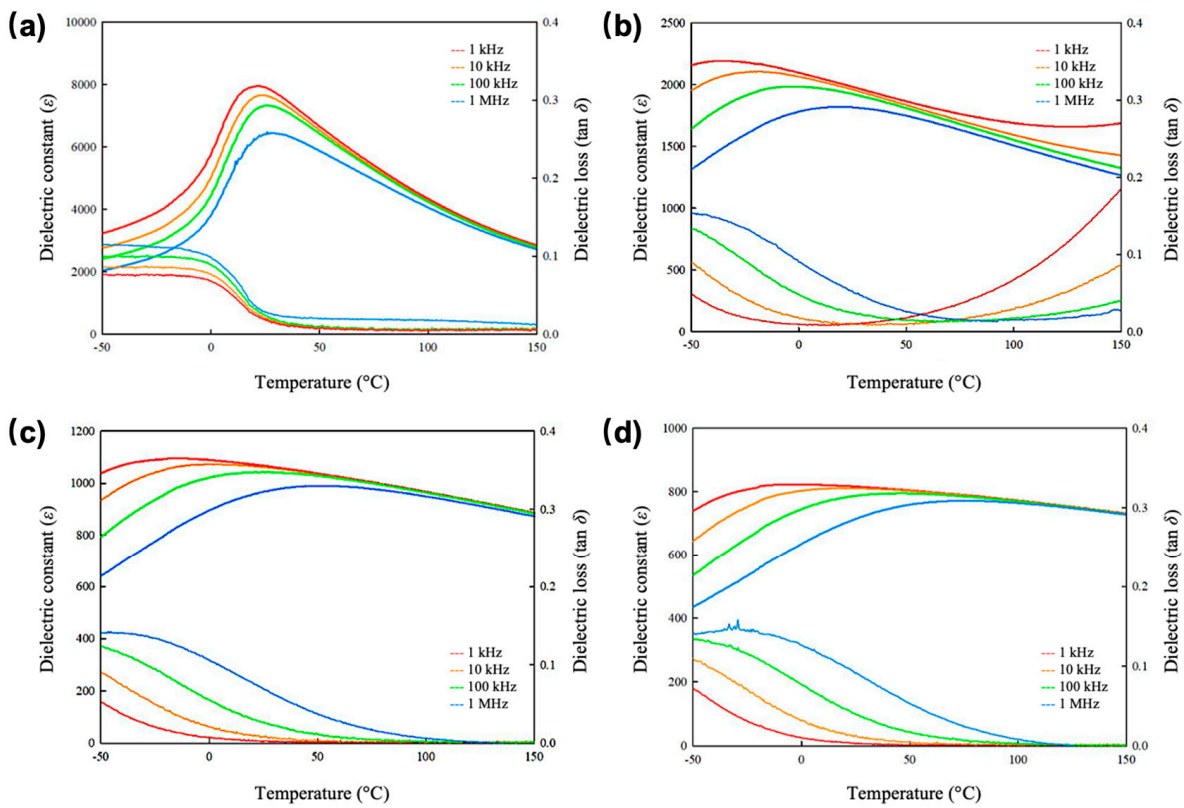


Figure 7. Dielectric behavior analysis of $(1-x)\text{BT}-x\text{Bi}(\text{Mg}_{1/3}\text{Zn}_{1/3}\text{Ta}_{1/6}\text{Nb}_{1/6})$ under $0.04 \leq x \leq 0.20$, $1 \text{ kHz} \leq f \leq 1 \text{ MHz}$, and $-50 \text{ }^{\circ}\text{C} \leq t \leq 150 \text{ }^{\circ}\text{C}$: (a) $x = 0.04$, (b) $x = 0.10$, (c) $x = 0.12$, and (d) $x = 0.20$.

These findings suggest that the introduction of doping elements in the $(1-x)\text{BT}-x\text{Bi}(\text{Mg}_{1/3}\text{Zn}_{1/3}\text{Ta}_{1/6}\text{Nb}_{1/6})$ system significantly influences the dielectric properties. The transition from the typical ferroelectric behavior of BT to the relaxor ferroelectric behavior is observed as the doping concentration increases, leading to a reduced dielectric constant and enhanced diffuse phase transition characteristics. This phenomenon can be attributed to the introduction of $(1-x)\text{BT}-x\text{Bi}(\text{Mg}_{1/3}\text{Zn}_{1/3}\text{Ta}_{1/6}\text{Nb}_{1/6})$ elements, which disrupt the long-range order of the Ti-O octahedra and induce local clustering of Ti^{4+} ions [21]. The resulting structural changes and the presence of ion-enriched regions contribute to the observed modifications in the dielectric behavior.

4.3. Impedance Analysis

Figure 8a $x = 0.04$, (b) $x = 0.10$, (c) $x = 0.12$, and (d) $x = 0.20$ shows the impedance analysis data of the four doping compositions in $(1-x)\text{BT}-x\text{Bi}(\text{Mg}_{1/3}\text{Zn}_{1/3}\text{Ta}_{1/6}\text{Nb}_{1/6})$ at different frequencies and temperatures. The horizontal axis represents the resistance (Z'), and the vertical axis represents the reactance (Z''). All the plots exhibit nearly semi-circular shapes. Due to the capacitive nature, Z' gradually decreases with increasing frequency; thus, the intersection of the semicircle with the x -axis in the low-frequency range represents the total resistance (R_{Total}) of the material at that temperature [26]. Additionally, the radius of the semicircle converges with the increasing temperature, indicating a decrease in impedance as the temperature rises. This is because the elevated temperature allows charge carriers to overcome the energy barrier more easily, resulting in decreased impedance and increased conductivity [27,28]. On the other hand, as the doping concentration increases, the enhancement in resistance also improves the material's withstand voltage, successfully addressing the low breakdown strength limitation of pure BT materials.

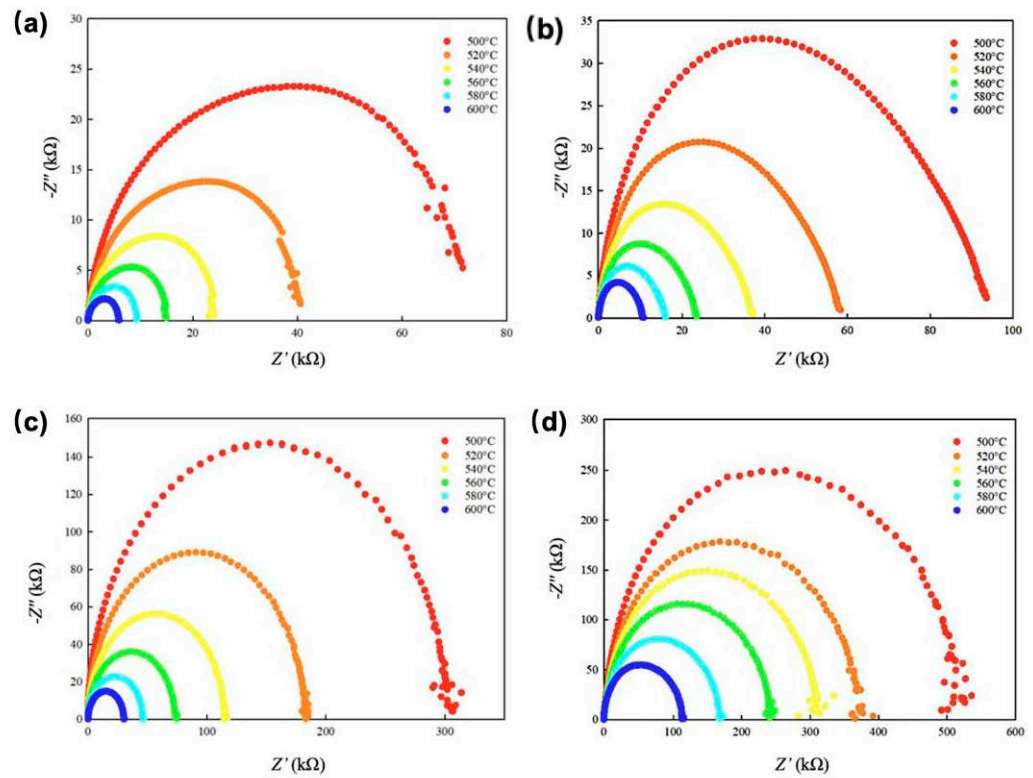


Figure 8. Impedance analysis data of the four doping compositions in $(1-x)\text{BT}-x\text{Bi}(\text{Mg}_{1/3}\text{Zn}_{1/3}-\text{Ta}_{1/6}\text{Nb}_{1/6})$ at different frequencies and temperatures: (a) $x = 0.04$, (b) $x = 0.10$, (c) $x = 0.12$, and (d) $x = 0.20$.

Figure 9 (a) $x = 0.04$, (b) $x = 0.10$, (c) $x = 0.12$, and (d) $x = 0.20$ shows the relationship between M''/M''_{max} and Z''/Z''_{max} for the four doping compositions. In an alternating electric field, the complex permittivity ϵ^* is defined as $\epsilon^* = \epsilon' - i\epsilon''$, where the real term corresponds to the capacitance and the complex term represents dielectric loss, given by $\tan \delta = \epsilon''/\epsilon'$ [28]. The complex modulus M^* is defined as $M^* = 1/\epsilon^* = \epsilon'/(\epsilon'^2 + \epsilon''^2) + i\epsilon''/(\epsilon'^2 + \epsilon''^2)$ [29]. In the BT perovskite structure, M'' primarily reflects grain response, while Z'' mainly represents grain boundary response [29,30]. The overlapping of the M''/M''_{max} and Z''/Z''_{max} peaks for $x = 0.12$ and $x = 0.20$ indicates a more homogeneous electrical structure in the latter case [31,32]. Furthermore, it is observed that the frequency corresponding to the peak value of M''/M''_{max} decreases with increasing doping concentration, demonstrating that doping is beneficial for reducing the material's conductivity [15]. From Figure 9, it can also be observed that the M''/M''_{max} and Z''/Z''_{max} peaks for $x = 0.12$ perfectly overlap, and the experimental energy storage data also show that $x = 0.12$ exhibits the optimal energy density and efficiency.

4.4. Polarization Measurements and Energy Storage Performance Analysis

Figure 10 shows the P - E curves of all compositions before reaching the breakdown field strength. The $x = 0.00$ composition represents the pure BT control group. From Figure 10a,b, it is evident that before $x < 0.08$, the hysteresis loop shape is significant, and the saturation polarization intensity (P_{max}) reaches over $32 \mu\text{C}/\text{cm}^2$, close to the P_{max} of $40 \mu\text{C}/\text{cm}^2$ for the pure BT group. However, it can be observed that the breakdown strength of $x < 0.08$, $180 \text{ kV}/\text{cm}$, is significantly higher than the $100 \text{ kV}/\text{cm}$ of the pure BT group, indicating that doping can effectively improve the susceptibility of BT-based ferroelectric ceramics to breakdown. Nevertheless, both $x < 0.08$ and pure BT exhibit high remanent polarization intensity (P_r), which affects the energy storage efficiency. As shown in Figure 11b, the energy density for $x = 0.00, 0.04$, and 0.05 is low, with the highest value reaching only $1 \text{ J}/\text{cm}^3$.

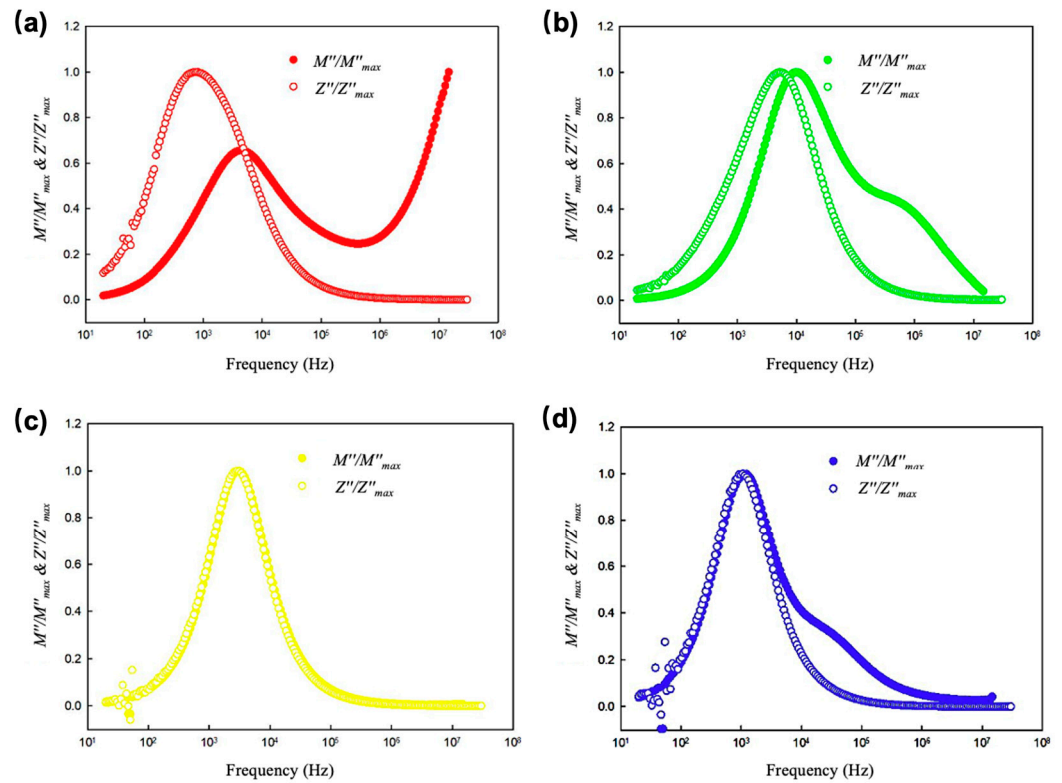


Figure 9. The relationship between M''/M''_{max} and Z''/Z''_{max} for the four doping compositions: (a) $x = 0.04$, (b) $x = 0.10$, (c) $x = 0.12$, and (d) $x = 0.20$.

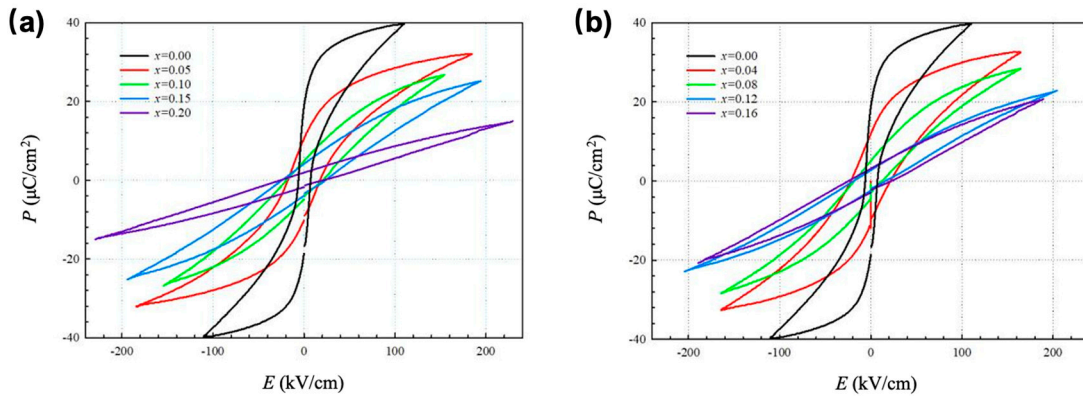


Figure 10. P - E curves of all compositions before reaching the breakdown field strength ($x = 0.00$ composition represents the pure BT control group): (a) $x = 0.05$ and derivative and (b) $x = 0.04$ and derivative.

As the doping ratio increases, the hysteresis loop for $0.08 \leq x \leq 0.20$ becomes noticeably narrower compared to $x < 0.08$. Moreover, as x increases, the slope of the curve decreases, resulting in a smoother hysteresis loop. Figure 11a reveals a significant reduction in spontaneous polarization intensity for $0.08 \leq x \leq 0.20$, not exceeding $5 \mu\text{C}/\text{cm}^2$, with $x = 0.12$ exhibiting the lowest value of only $3 \mu\text{C}/\text{cm}^2$. Figure 10b also indicates that the $x = 0.12$ composition performs the best, with an energy density of $1.75 \text{ J}/\text{cm}^3$ and an efficiency of 75%.

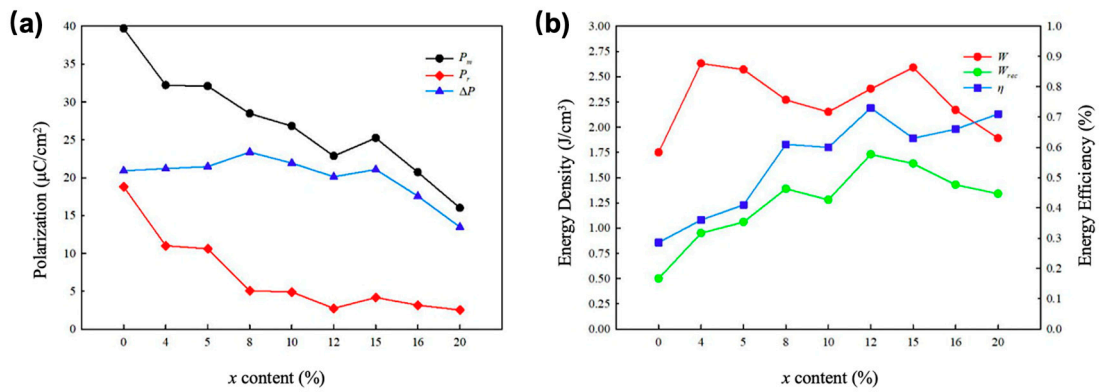


Figure 11. Polarization intensity line graphs for (a) P_{max} and P_r and (b) energy density and efficiency for all components ($0.08 \leq x \leq 0.20$).

The BT sample with $x = 0.12$ is considered the best in terms of energy density due to the increasing breakdown strength. As seen in Figure 11a, although the saturation polarization intensity (P_{max}) generally decreases linearly with the increasing doping level (x), the energy density reaches its peak at $x = 0.12$. However, as P_{max} decreases rapidly beyond this point, the energy density subsequently decreases as well. This indicates that the optimal doping level of $x = 0.12$ provides a balance between increasing breakdown strength and maintaining a high energy density.

To further explore the relationship between doping level (x) and polarization (P), the P - E curve at $E = 120 \text{ kV}/\text{cm}$ is selected. Figure 12 presents the P - E curves for all compositions at this electric field. As x increases from 0.04 to 0.20, the curves become flatter with lower slopes, indicating a gradual decrease in the saturation polarization intensity (P_{max}) under the same electric field. Comparing Figures 10 and 12 reveals that as the applied electric field (E) increases, the hysteresis loop becomes larger, resulting in a reduction in energy storage efficiency.

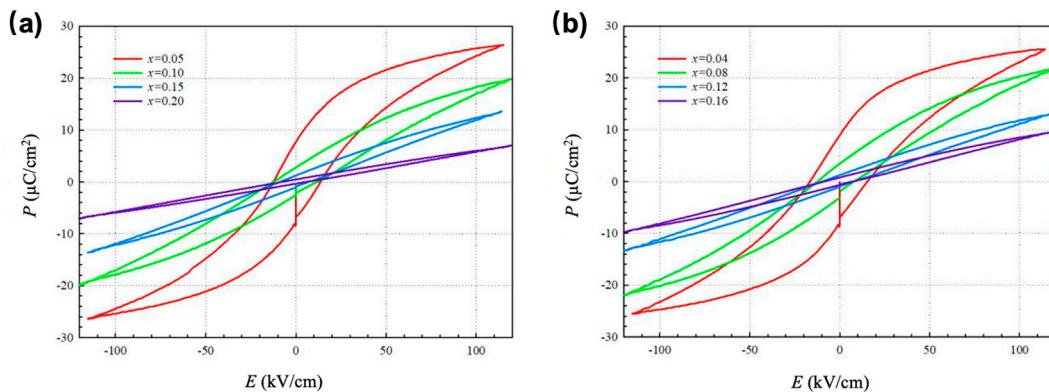


Figure 12. P - E curves of all compositions at $E = 120 \text{ kV}/\text{cm}$ ($x = 0.00$ composition represents the pure BT control group): (a) $x = 0.05$ and derivative and (b) $x = 0.04$ and derivative.

Figure 13a displays the P_{max} and P_r values for all compositions at $E = 120 \text{ kV}/\text{cm}$, while Figure 13b illustrates the corresponding energy density and efficiency. Based on Figure 13b, it can be concluded that under the same external electric field, the energy storage efficiency increases with increasing x , ranging from 37% for $x = 0.04$ to 86% for $x = 0.20$. However, it should be noted that the polarization intensity of $x = 0.20$ is too low for practical applications, limiting its effectiveness as a dielectric energy storage material. On the other hand, the energy density of the $x = 0.12$ composition is more than 50% higher, making it the most favorable choice in terms of achieving a balance between high energy density and acceptable polarization intensity.

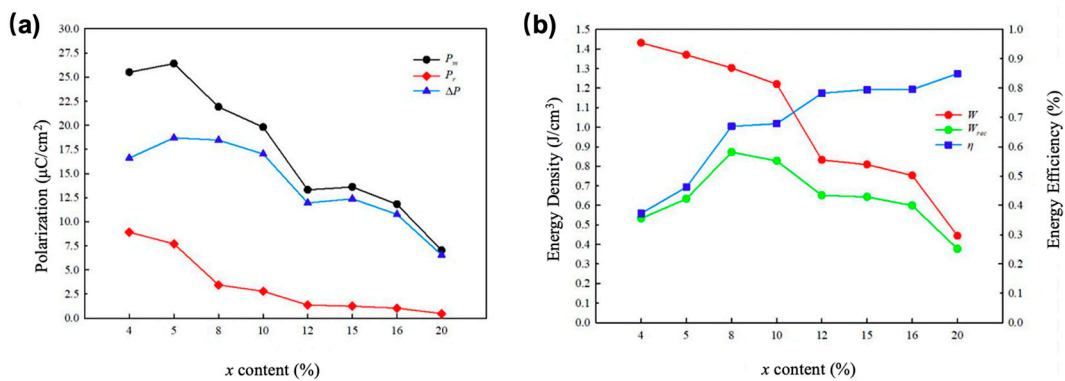


Figure 13. Polarization intensity line graphs at $E = 120$ kV/cm for (a) P_{max} and P_r and (b) energy density and efficiency for all components ($0.08 \leq x \leq 0.20$).

5. Limitation and Future Works

Despite the significant findings obtained in this study, there are several limitations that should be addressed in future research. Firstly, the combination of doping elements at the B-site was kept constant throughout the experiments, with Bi^{3+} and Zn^{2+} being the selected dopants. However, exploring different ratios and combinations of dopants could provide valuable insights into the influence of specific dopants on the structural and energy storage properties of the BT–Bi solid solution. Different dopants may exhibit varying degrees of chemical compatibility, lattice distortion, and charge compensation effects, which can impact the overall performance of the material. Further investigations with varying dopant ratios and incorporating additional dopants, such as La^{3+} or Nb^{5+} , can offer a more comprehensive understanding of the doping mechanisms and optimize the energy storage capabilities.

Secondly, the data collection in this study was limited to a comparative analysis of eight compositions with the same AB substitution mode, namely, $(1-x)\text{BT}-x\text{Bi}(\text{Mg}_{1/3}\text{Zn}_{1/3}\text{Ta}_{1/6}\text{Nb}_{1/6})$. While this approach provides valuable insights into the influence of different doping levels, exploring other substitution modes and a wider range of compositions could yield additional information. Investigating alternative substitution modes, such as $(1-x)\text{BT}-x\text{Bi}(\text{Mg}_{1/2}\text{Zn}_{1/2})\text{O}_3$ or $(1-x)\text{BT}-x\text{Bi}(\text{Mg}_{1/2}\text{Zn}_{1/2})\text{NbO}_3$, may lead to different structural arrangements and further enhance the energy storage properties. Furthermore, incorporating a broader range of doping levels and exploring the compositional space beyond the investigated range ($x = 0.04-0.20$) can provide a more comprehensive understanding of the material’s behavior and its potential for further improvement.

Additionally, it is important to address the limitations associated with the ferroelectric testing procedure employed in this study. The need to grind the samples to a thickness of 0.2 mm before testing may introduce unintended damage and alter the material’s properties. This grinding process can potentially affect the structural integrity, surface morphology, and electrical properties of the samples. Future studies should consider alternative characterization techniques that allow non-destructive testing, such as piezoelectric force microscopy or electrical impedance spectroscopy, to analyze the material’s properties without the need for sample thinning. These techniques can provide valuable insights into the local domain structure, polarization behavior, and energy storage performance of the ceramics, while preserving the integrity of the samples.

In conclusion, while this study provides important insights into the doping effects on the structural characteristics, relaxation phenomena, and energy storage performance of the new ceramics, there are several avenues for future research. Exploring different dopant combinations and ratios, investigating alternative substitution modes, expanding the composition range, and employing non-destructive testing methods will contribute to a more comprehensive understanding of the material and facilitate the optimization of its energy storage properties for practical applications.

6. Conclusions

In conclusion, this study successfully investigated the structural characteristics, relaxation phenomena, and energy storage performance of $(1-x)\text{BT}-x\text{Bi}(\text{Mg}_{1/3}\text{Zn}_{1/3}\text{Ta}_{1/6}\text{Nb}_{1/6})$ ceramics. By doping the pure BT ceramics with Bi^{3+} , Zn^{2+} , and other elements, eight different compositions ($x = 0.04, 0.05, 0.08, 0.10, 0.12, 0.15, 0.16, 0.20$) were synthesized using solid-state sintering. The results confirmed the transformation of the BT perovskite structure from a tetragonal phase to a pseudocubic phase with doping, as verified by XRD and Raman spectroscopy. The introduction of dopants led to the emergence of relaxation ferroelectric behavior, as evidenced by broad and flat dielectric peaks and frequency dispersion in the spectra. The doping ratio x had a significant influence on the dielectric properties, with larger dopant concentrations resulting in lower dielectric constants and consistently low dielectric loss. The ferroelectric testing demonstrated that doping significantly improved the energy storage efficiency, reduced energy losses during charge–discharge cycles, and enhanced the breakdown strength, increasing the maximum electric field from 100 kV/cm for pure BT ceramics to 180–200 kV/cm. Moreover, the energy storage efficiency increased with higher dopant concentrations, from 37% for $x = 0.04$ to 86% for $x = 0.20$, at the same electric field. Impedance analysis and energy storage characterization both indicated that the composition with $x = 0.12$ exhibited the best performance, achieving a maximum field strength of $E = 203$ kV/cm with energy density and efficiency values of 1.75 J/cm³ and 75%, respectively. Nonetheless, further research is needed to explore different dopant combinations, expand the composition range, and employ non-destructive testing methods to overcome the limitations encountered in this study.

Author Contributions: Conceptualization, J.S. and Y.L.; methodology, Y.L.; software, J.S.; validation, J.S. and Y.L.; formal analysis, J.S.; investigation, J.S.; resources, J.S.; data curation, Y.L.; writing—original draft preparation, J.S.; writing—review and editing, Y.L.; visualization, Y.L.; supervision, Y.L.; project administration, J.S.; funding acquisition, Y.L. All authors have read and agreed to the published version of the manuscript.

Funding: This research was funded by Enerstay Sustainability Pte Ltd. (Singapore) Grant Call (Call 1/2022)_GHG (Project ID VS1-001), Singapore.

Institutional Review Board Statement: Not applicable.

Informed Consent Statement: Not applicable.

Data Availability Statement: The data that support the findings of this study are available from the corresponding author upon reasonable request.

Conflicts of Interest: The authors declare no conflict of interest.

References

1. Winter, M.; Brodd, R.J. What are batteries, fuel cells, and supercapacitors? *Chem. Rev.* **2004**, *104*, 4245–4270. [[CrossRef](#)] [[PubMed](#)]
2. Han, K.; Li, Q.; Chen, Z.; Gadinski, M.R.; Dong, L.; Xiong, C.; Wang, Q. Suppression of energy dissipation and enhancement of breakdown strength in ferroelectric polymer-graphene percolative composites. *J. Mater. Chem. C* **2013**, *1*, 7034–7042. [[CrossRef](#)]
3. Yang, L.T.; Kong, X.; Li, F.; Hao, H.; Cheng, Z.; Liu, H.; Li, J.-F.; Zhang, S. Perovskite lead-free dielectrics for energy storage applications. *Prog. Mater. Sci.* **2019**, *102*, 72–108. [[CrossRef](#)]
4. Chu, B.J.; Zhou, X.; Ren, K.L.; Neese, B.; Lin, M.; Wang, Q.; Bauer, F.; Zhang, Q.M. A dielectric polymer with high electric energy density and fast discharge speed. *Science* **2006**, *313*, 334–336. [[CrossRef](#)]
5. Whittingham, M.S. Materials challenges facing electrical energy storage. *MRS Bull.* **2008**, *33*, 411–419. [[CrossRef](#)]
6. Liu, Z.; Lu, T.; Ye, J.M.; Wang, G.; Dong, X.; Withers, R.; Liu, Y. Antiferroelectrics for energy storage applications: A review. *Adv. Mater. Technol.* **2018**, *3*, 1800111. [[CrossRef](#)]
7. Hao, X.H. A review on the dielectric materials for high energy-storage application. *J. Adv. Dielectr.* **2013**, *3*, 1330001. [[CrossRef](#)]
8. Yao, Z.H.; Song, Z.L.; Hao, H.; Yu, Z.; Cao, M.; Zhang, S.; Lanagan, M.T.; Liu, H. Homogeneous/inhomogeneous-structured dielectrics and their energy-storage performances. *Adv. Mater.* **2017**, *29*, 1601727. [[CrossRef](#)]
9. Li, Q.; Han, K.; Gadinski, M.R.; Dong, L.; Xiong, C.; Wang, Q. High energy and power density capacitors from solution-processed ternary ferroelectric polymer nanocomposites. *Adv. Mater.* **2014**, *26*, 6244–6249. [[CrossRef](#)]
10. Xiao, S.; Xiu, S.M.; Shen, B.; Zhai, J. Microstructure evolution and energy storage of potassium strontium niobate boroaluminosilicate glass-ceramics by microwave crystallization. *J. Eur. Ceram. Soc.* **2016**, *36*, 4071–4076. [[CrossRef](#)]

11. Wang, Y.F.; Cui, J.; Yuan, Q.B.; Niu, Y.; Bai, Y.; Wang, H. Significantly enhanced breakdown strength and energy storage in sandwich-structured Barium Titanate/Poly(vinylidene fluoride) nanocomposites. *Adv. Mater.* **2015**, *27*, 6658–6663. [[CrossRef](#)] [[PubMed](#)]
12. Zhong, W.L. *Ferroelectric Physics*; Science Press: Beijing, China, 1996.
13. Wu, Z.; Cohen, R.E. Pressure-induced anomalous phase transitions and colossal enhancement of piezoelectricity in PbTiO_3 . *Phys. Rev. Lett.* **2005**, *95*, 037601. [[CrossRef](#)] [[PubMed](#)]
14. Zhu, L.F. Phase Structure Regulation and Performance Enhancement Mechanism of High-Performance Lead-Free Barium Titanate-Based Piezoelectric Ceramics. Ph.D. Thesis, University of Science and Technology Beijing, Beijing, China, 2015.
15. Wang, X. Study on the Dielectric Energy Storage Characteristics of Barium Titanate-Based Ferroelectric Ceramics. Ph.D. Thesis, Shandong University, Jinan, China, 2020.
16. Duan, X.; Luo, W.; Wu, W.; Yuan, J. Dielectric response of ferroelectric relaxors. *Solid State Commun.* **2000**, *114*, 597–600. [[CrossRef](#)]
17. Tang, B. Research on the Development and Modification Mechanism of Temperature-Stable MLCC Ceramic Materials. Ph.D. Thesis, University of Electronic Science and Technology of China, Chengdu, China, 2008.
18. Guo, H.F.; Chen, X.M. Raman spectroscopy study of BaTiO_3 ferroelectric phase transition. *J. Jiaozuo Univ.* **2003**, *17*, 35–37.
19. Yue, Y.; Lu, D.Y. Influence of strontium doping on structural phase transition and Raman charge effect of lanthanum barium titanate ceramics. *J. Jilin Inst. Chem. Technol.* **2013**, *30*, 42–44.
20. Yang, J.L. Study on the Dielectric Stability of Barium Titanate-Based Ceramics. Ph.D. Thesis, National University of Defense Technology, Changsha, China, 2019.
21. Jin, L.; Li, F.; Zhang, S. Decoding the Fingerprint of Ferroelectric Loops: Comprehension of the Material Properties and Structures. *J. Am. Ceram. Soc.* **2014**, *97*, 1. [[CrossRef](#)]
22. Kreisel, J.; Bouvier, P.; Maglione, M.; Dkhil, B.; Simon, A. High-pressure Raman investigation of the Pb-free relaxor $\text{BaTi}_{0.65}\text{Zr}_{0.35}\text{O}_3$. *Phys. Rev. B* **2004**, *69*, 092104. [[CrossRef](#)]
23. Hu, Q.; Bian, J.; Zelenovskiy, P.S.; Hu, Q.; Bian, J.; Zelenovskiy, P.S.; Tian, Y.; Jin, L.; Wei, X.; Xu, Z.; et al. Symmetry changes during relaxation process and pulse discharge performance of the $\text{BaTiO}_3\text{-Bi}(\text{Mg}_{1/2}\text{Ti}_{1/2})\text{O}_3$ ceramic. *J. Appl. Phys.* **2018**, *124*, 054101. [[CrossRef](#)]
24. Yang, L.Y.; Li, X.Y.; Allahyarov, E.; Taylor, P.L.; Zhang, Q.M.; Zhu, L. Novel polymer ferroelectric behavior via crystal isomorphism and the nanoconfinement effect. *Polymer* **2013**, *54*, 1709–1728. [[CrossRef](#)]
25. Raengthon, N.; DeRose, V.J.; Brennecke, G.L.; Cann, D.P. Defect mechanisms in high resistivity $\text{BaTiO}_3\text{-Bi}(\text{Zn}_{1/2}\text{Ti}_{1/2})\text{O}_3$ ceramics. *Appl. Phys. Lett.* **2012**, *101*, 112904. [[CrossRef](#)]
26. Shamim, M.K.; Sharma, S.; Singh, A.; Rai, R.; Rani, R. Study of the structural and electrical behavior of $\text{Bi}(\text{Mg,Ti})\text{O}_3$ modified $(\text{Ba,Ca})\text{TiO}_3$ ceramics. *J. Adv. Dielectr.* **2016**, *6*, 1650035. [[CrossRef](#)]
27. Li, Z.; Fan, H. Polaron relaxation associated with the localized oxygen vacancies in $\text{Ba}_{0.85}\text{Sr}_{0.15}\text{TiO}_3$ ceramics at high temperatures. *J. Appl. Phys.* **2009**, *106*, 054102. [[CrossRef](#)]
28. Elissalde, C.; Ravez, J. Ferroelectric ceramics: Defects and dielectric relaxations. *J. Mater. Chem.* **2001**, *11*, 1957–1967. [[CrossRef](#)]
29. Sinclair, D.C.; West, A.R. Impedance and modulus spectroscopy of semiconducting BaTiO_3 ; showing positive temperature coefficient of resistance. *J. Appl. Phys.* **1989**, *66*, 3850–3856. [[CrossRef](#)]
30. Hirose, N.; West, A.R. Impedance Spectroscopy of Undoped BaTiO_3 Ceramics. *J. Am. Ceram. Soc.* **1996**, *79*, 1633–1641. [[CrossRef](#)]
31. Muhammad, R.; Iqbal, Y.; Reaney, I.M. $\text{BaTiO}_3\text{-Bi}(\text{Mg}_{2/3}\text{Nb}_{1/3})\text{O}_3$ Ceramics for High-Temperature Capacitor Applications. *J. Am. Ceram. Soc.* **2016**, *99*, 2089–2095. [[CrossRef](#)]
32. Chen, J.X. Synthesis and Properties of Perovskite Oxides Based on Barium Titanate. Ph.D. Thesis, East China Normal University, Shanghai, China, 2022.

Disclaimer/Publisher’s Note: The statements, opinions and data contained in all publications are solely those of the individual author(s) and contributor(s) and not of MDPI and/or the editor(s). MDPI and/or the editor(s) disclaim responsibility for any injury to people or property resulting from any ideas, methods, instructions or products referred to in the content.